Modes of ejecta emplacement at Martian craters from laboratory experiments of an expanding vortex ring interacting with a particle layer

A Suzuki, I Kumagai, Y Nagata, K Kurita, Olivier S. Barnouin-Jha

Modes of ejecta emplacement at Martian craters from laboratory experiments of an expanding vortex ring interacting with a particle layer

A. Suzuki,[1] I. Kumagai,[2] Y. Nagata,[3] K. Kurita,[1] and O. S. Barnouin-Jha[4]

[1] Ejecta morphologies of many Martian craters indicate fluidized emplacement which differs from ballistic emplacement in dry, airless environments. Double Layered Ejecta craters possess particularly interesting ejecta morphologies: two lobes and radial lineations on their surface, which probably result from gas-dominated radial flow during the emplacement. To examine how a radial flow interacts with surface particles to generate some of the observed morphologies on Mars, we have conducted water tank experiments in which a vortex ring encounters a particle layer. The threshold of particle motion and three interaction modes are described by two dimensionless numbers: particle Shields' parameter and particle Reynolds number. Our results show that gas-dominated flows are possible during cratering and could be used to constrain the ancient Martian environment from observations. **Citation:** Suzuki, A., I. Kumagai, Y. Nagata, K. Kurita, and O. S. Barnouin-Jha (2007), Modes of ejecta emplacement at Martian craters from laboratory experiments of an expanding vortex ring interacting with a particle layer, *Geophys. Res. Lett.*, *34*, L05203, doi:10.1029/2006GL028372.

1. Introduction

[2] Ejecta morphologies of impact craters on Mars are different from those of craters on other planets, which are formed by ballistic sedimentation. The distinctive morphologies of Martian ejecta suggest radial ground-hugging flows during deposition [e.g., *Carr et al.*, 1977], which are generally attributed to the presence of fluids such as the Martian atmosphere [e.g., *Schultz*, 1992; *Barnouin-Jha and Schultz*, 1998] and/or subsurface volatiles [e.g., *Carr et al.*, 1977]. A third possibility, namely a simple granular flow, could also form the observed morphologies without direct inclusions of water or atmosphere [*Wada and Barnouin-Jha*, 2006]. In all instances, questions still remain on what processes and materials contribute to ejecta fluidization and sedimentation.

[3] High-quality data obtained by recent Mars exploration has revealed new aspects of the formation processes of Martian crater ejecta. Some Martian craters have numerous radial lineations on the surface of their ejecta [*Mouginis-*

Mark, 1981; *Boyce and Mouginis-Mark*, 2006]. These craters are classified as Double Layered Ejecta (DLE) craters [*Barlow et al.*, 2000] because their ejecta consist of two facies: a thick and concave inner lobe and a faint outer lobe without distal ramparts. While it has been proposed that two different processes dominate the formation of all fluidized ejecta on Mars [*Schultz*, 1992; *Barnouin-Jha et al.*, 2005], the ejecta facies of the inner and outer lobe of DLE craters differ so significantly that these are particular good candidates for identifying the two processes [*Mouginis-Mark*, 1981]. The radial lineations, which cross the margin of the inner lobe [*Boyce and Mouginis-Mark*, 2006], indicate a late-stage radial flow that scours the inner lobe after its emplacement [*Mouginis-Mark*, 1981]. The radial flows could be gas-dominated because large boulders and masses of materials at the terminus of the lineations are not observed. Dry granular flows could form the fluidized ejecta, however it could not form layered ejecta [*Wada and Barnouin-Jha*, 2006].

[4] Models of a radial gas-dominated flow generated at late stages during impact cratering have been proposed following either the collapse of an ejecta plume generated from a volatile-rich target [e.g., *Mouginis-Mark*, 1981] or a vortex ring generated from atmospheric flow behind an ejecta curtain [e.g., *Schultz*, 1992; *Barnouin-Jha and Schultz*, 1996, 1998]. Experimental studies that demonstrate radial flows are limited, although an expanding vortex ring at the late stage of cratering has been seen in a series of impact cratering experiments [*Schultz*, 1992; *Barnouin-Jha and Schultz*, 1996]. Visualization of fluid motion is rather difficult because the experimental time scale using air is quite short [*Barnouin-Jha and Schultz*, 1996; *Greeley*, 2002].

[5] In order to understand the formation process of the observed morphology of the Martian crater ejecta, it is first necessary to investigate the basic physics of the particle movement in the radial flows. Although the threshold for displacement of particles by flows over the particle layers has been well documented since the 1940's [e.g., *Bagnold*, 1941], most experiments have been performed in a wind tunnel where the wind has a steady unidirectional velocity profile. The situation of the radial flows is rather complicated because the flow velocity decreases with distance from the center and circumferential instabilities form [*Barnouin-Jha and Schultz*, 1998; *Widnall et al.*, 1974]. The details of how these types of flow evolve and interact with sediments require further study.

[6] This paper examines the interaction of an expanding vortex ring with a particle layer by means of laboratory experiments. We consider only the late stages of ejecta

---
[1]Earthquake Research Institute, University of Tokyo, Tokyo, Japan.
[2]Institut de Physique du Globe de Paris, Paris, France.
[3]Department of Applied Physics, Tokyo University of Agriculture and Technology, Tokyo, Japan.
[4]Johns Hopkins University Applied Physics Laboratory, Laurel, Maryland, USA.
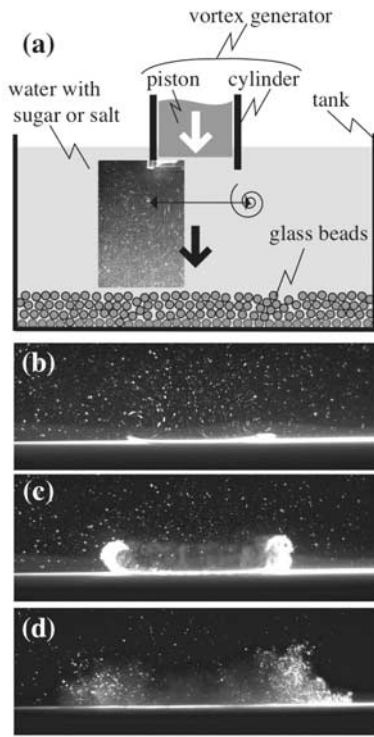
Figure 1. (a) A cross-sectional schematic view of the experimental equipment. The size of the tank is 36×25, 26.4 cm high. By moving the piston downward (white arrow), a vortex ring was generated, which translated toward the particle layer at the bottom (black arrows). The two-headed arrow indicates the distance between vortex core centers. (b, c, d) Typical sequential images of lift mode ($\theta_p \sim 49$, $Re_p \sim 19$). Each image is 0.056, 0.171, 0.915 sec after the vortex ring started to entrain particles, respectively. Particles tracks in the vortex ring are visualized by digital summation of successive 8 (Figure 1b) and 4 (Figure 1c) frames. The bright horizontal line is the surface of particle layer. Note that the particle are not homogeneously lifted by the vortex ring.

emplacement responsible for the previously described morphologies, where early-time cratering effects due to the formation of the ejecta plume, vapor cloud, and wake trailing the projectile should have little influence [*Schultz*, 1992]. Because of the visualization difficulties mentioned above, we therefore use water in our experiments as a substitute for air. We show a regime diagram based on the resultant morphologies of the particle layer and discuss the particle threshold problems. We then extrapolate our results to Mars.

2. Experimental Equipment and Method

[7] The experiments were conducted in a transparent rectangular tank filled with tap water (Figure 1a). We placed particles at the bottom of the tank, and made their surface flat. The radial flows we investigated originated from a vortex ring which impacted on the particle layer, like the radial flows that might be expected from plume collapse or impact-derived winds at the late stages of cratering. The

vortex ring generator, composed of a piston and a cylinder, was placed in the upper part of the tank. Moving the piston downwards generated a single vortex ring. The vortex ring descended with nearly constant velocity until it approached to the particle layer at the bottom of the tank, and then expanded radially over the layer (Figure 1b). Subsequently, the vortex ring reduced its radial velocity with time interacting with the particles. Note that there is no crater cavity in our experiments because our experiments are designed to investigate the physics of the interaction of radial flows with a particle layer, to understand how late-stage impact-derived winds or plumes interact with a previously emplaced ejecta and/or a target surface.

[8] In order to measure the diameter and translational velocity of the vortex ring, fine-grained tracers with neutral buoyancy (50 μm in diameter) were added in water, and a vertical laser sheet illuminated the tank. We monitored the experiments with both a commercial digital video camera and a high-speed digital video camera (1024×1024 pixels at 1000 frames/sec). We measured the diameter and the translational velocity of the vortex ring in vertical plane, which is the distance between the centers of vortex cores and the trajectory of them, respectively (Figure 1a). We also took pictures of the particle layer from above, and observed how its morphology was modified by the vortex ring.

[9] The experimental conditions are summarized in Table 1. Both the diameter d of the particles and densities of the water ρ_{flow} were changed. We added sugar or salt to the fluid to control the normalized density difference $\Delta\rho^* = (\rho_{particle} - \rho_{flow})/\rho_{flow}$. The initial translational velocity of the vortex ring U was varied by controlling both the downward velocity and displacement of the piston. The initial radius was controlled by using three vortex generators with different diameters (cylinder diameter: 51.9 mm, 64.9 mm, 85.7 mm). The kinematic viscosity of the water ν at room temperature (20 degrees centigrade) is 1.004×10^{-6} m^2/s, which is used for our calculation.

3. Results

3.1. Surface Morphologies

[10] After the vortex ring reaches the particle layer, its shape is deformed and its diameter increases with time. The resultant morphologies vary both with U and $\Delta\rho^*$. These variations are mainly due to the threshold of particle motion. Based on the modified morphologies, we classify the

Table 1. Parameters Used in These Experiments[a]

Parameters	Values
Particles ($\rho_{particle}$, g/cm^3, d, mm)	(2.460, 0.1)
	(1.372, 2.2)
	(1.361, 5.1)
	(1.056, 1.0)
	(1.025, 1.5)
	(1.021, 6.0)
ρ_{flow}, g/cm^3	0.99, 1.00, 1.02
U_{vortex}, mm/s	$3.4 \sim 244$
Re_{vortex}	$2.9 \times 10^2 \sim 1.5 \times 10^4$

[a]$\rho_{particle}$ and ρ_{flow} are the densities of the particles and the fluid, respectively. d is the mean diameter of the particles. U is the initial translational velocity of a vortex ring. $Re_{vortex} = UD_c/\nu$ is the Reynolds number of a vortex ring, where D_c is the inner diameter of cylinder, which is comparable to the initial diameter of the vortex ring.
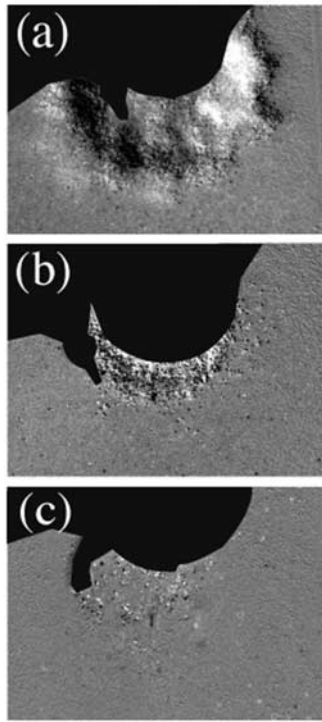
Figure 2. Typical results of each mode. Each image is obtained by subtracting two images before and after the interaction. The black filled area (upper part of the images) is the vortex generator. (a) The morphology in lift mode has a petal-like circumference, which resembles Martian fluidized ejecta. (b) The morphology in slide mode shows nearly circular features. Petal-like shape is not observed. (c) Nothing happens on the surface of particle layer in the no-motion mode.

experimental results into three modes: a lift mode, a slide mode, and a no-motion mode (Figure 2).

[11] The resultant morphologies in the lift mode are petal shaped with two facies: a circular scoured facies located in the center and petal-like depositional facies surrounding the scoured facies (Figure 2a). The petal-like shape is one of the notable features of this morphology. When the vortex ring reaches the particle layer, it scours the surface of the layer and lifts the particles (Figures 1b and 1c). The suspended particles are transported outwards by the radial flow, and deposited on the outside of the inner scoured facies because the radial velocity of the vortex ring decreases as it expands (Figure 1d). It is observed that the number of suspended particles is inhomogeneous in azimuthal direction (Figure 1c), which would result from a circumferential instability of the vortex ring [e.g., *Widnall et al.*, 1974]. The higher-velocity segments in the instability of the vortex ring entrain more grains and lift them up to higher position. This high-density clouds collapse spontaneously to form gravity currents, which extend to a long distance (Figure 1d). Radial lineations are also observed on the surface of the particle layer. As a result, the particles are deposited in a sinuous, petal-like shape, and inner scoured facies with radial lineations and outer depositional facies are formed in a single interaction between a vortex ring and a particle layer, which resembles the Martian DLE craters. All

these processes and many of the observed morphologies are also observed during the transport and deposition of ejecta in impact experiments in an atmosphere [*Schultz*, 1992; *Barnouin-Jha and Schultz*, 1996].

[12] In the slide mode, the resultant morphologies are nearly circular; the petal-like depositional facies observed in the lift mode are not formed (Figure 2b). The particles near the surface are only scoured and swept by the radial flow of the expanding vortex ring because U is not fast enough and/or $\Delta\rho*$ is not small enough to lift particles. In the no-motion mode, nothing happens on the surface of the particle layer (Figure 2c). A vortex ring would be incapable of displacing any particles because U is too slow and/or $\Delta\rho*$ is large.

3.2. Threshold of Particle Motion and Regime Diagram

[13] The mobility of a particle depends on the balance between the drag force and the gravity force acting on it [*Bagnold*, 1941]. The three modes observed in our experiments can be related to two dimensionless numbers which take into account this balance: the particle Shields' parameter $\theta_p = U^2/\Delta\rho* gr$ and particle Reynolds number $Re_p = 2 Ur/\nu$. The variables r, g, and ν are the radius of the particles, the gravitational acceleration, and the kinematic viscosity of the ambient fluid, respectively; U is used to represent a characteristic velocity. The Shields' parameter is the ratio of the inertial forces that lift and move a particle, to the gravitational buoyancy forces that pull it down. The Reynolds number parameterizes these same inertial forces relative to the viscous drag acting on the particle. *Eames and Dalziel* [2000] found that both θ_p and Re_p are natural parameters for describing the collision between a wake generated by a sphere with a particulate surface.

[14] Figure 3a presents the regimes in which our observed modes dominate as a function of Re_p and θ_p. This regime diagram shows that when Re_p and θ_p are large, the particles are easily moved by the radial flows of vortex ring and the morphologies resulting from either the lift mode or slide mode are obtained. In Figure 3a, the boundaries of each mode seem to depend on Re_p for small Re_p, while they seem to be constant for large Re_p. *Eames and Dalziel* [2000] conclude that the relation between the thickness of the velocity boundary layer δ and particle diameter d can account for the variation of the dependence on Re_p. If $\delta < d$ (for large Re_p), the magnitude of the fluid velocity over the particle will be on the order of U and the threshold of particle motion $\theta_{SM \cdot NM}$ should be no dependence on Re_p. However, if $\delta > d$ (for small Re_p), the characteristic flow velocity over the particle will be on the order of $(U^2 d/\nu)$ and $\theta_{SM \cdot NM} \sim Re_p^{-2}$ is expected. In the context of this discussion, we draw two critical curves, $\theta_{LM \cdot SM}$ and $\theta_{SM \cdot NM}$, which correspond to the thresholds for particle motion and lifting, respectively. These two curves reasonably delineate each modes of our experimental data, and they seem to bend around $Re_p \sim 50$, although more data are probably required to confirm this result statistically.

4. Discussion

[15] We now extrapolate our laboratory results to the Martian environment (Table 2). In our analysis, we assume that the present day Martian atmosphere is well represented by CO_2 gas. For simplicity, we ignore any prior effects of
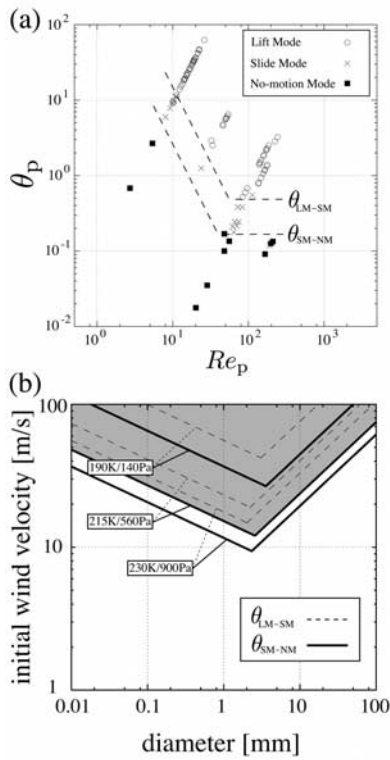
Figure 3. (a) Regime diagram as a function of θ_p and Re_p. Definition of these parameters are given in the text. (b) Regime diagram as a function of particle diameter d and initial wind velocity of the radial flow U. Parameters used in this diagram are listed in Table 2, which represent present Martian conditions. The shaded area corresponds to the lift and slide modes presented at 215 K/560 Pa, and displays the condition for particle motion.

on the vortex ring diameter (Re_{vortex} in Table 1) is far smaller in the laboratory than on Mars. It could have some effect on the use of U as the characteristic flow velocity since expected enhancements in turbulence in the flow may cause more rapid dissipations.

[16] The threshold wind velocity has been extensively studied not only on Earth [e.g., *Bagnold*, 1941] but also on Mars and other planets [e.g., *Sagan*, 1975; *Sagan and Bagnold*, 1975]. Our regime diagram (Figure 3b) is consistent with these studies in wind velocity [e.g., *Greeley et al.*, 1980, Figure 5]: the threshold velocities are of the order of ~10 m/s. However, the particle size most easily moved by wind is inconsistent with these previous results. The optimum diameter for minimum threshold in Figure 3b is ~2 mm, approximately a factor of 10 larger than previous results determined in wind tunnels. This difference could be due to the different flow geometries: flows in our vortex rings have both vertical and radial (horizontal) components, while flows demonstrated in the wind tunnel experiments have only unidirectional (horizontal) component. The vertical (upward) component in the front side of the expanding vortex ring should promote the particles to move and easily lift them off the surface. Furthermore, vortex stretching effects associated with the conservation of angular flow speed in the vortex can initially cause an increase in the flow speeds in the vortex ring, namely these vertical components. In addition, secondary vortices are generated resulting from circumferential instabilities in the vortex ring that grow as a result of interactions with the surface, and could also help the large particles to move. Note that small particles are less affected by these vortices because turbulent motion associated with the secondary vortices is small near a wall.

[17] Considering more realistic Martian conditions, the radial vortex flow could be denser than the ambient atmosphere because of previous entrainment of fine-grained atmospheric heating or particle loading [e.g., *Barnouin-Jha and Schultz*, 1998] which could occur during a real impact event, by assuming that the density of the radial flow in the vortex ring is the same as the ambient CO_2 atmosphere. Figure 3b is a regime diagram as a function of initial wind velocity U and particle diameter d in the present Martian environment (215 K/560 Pa). We also show the cases of 190 K/140 Pa and 230 K/900 Pa in the same diagram. The former corresponds to the approximated value at 15 km in height at which the ejecta of DLE craters could reach and the latter is the maximum value observed in the Viking mission [*Zurek*, 1992]. The shaded area corresponds to the lift and slide modes and indicates the conditions of U and d required for particle motion. Our result supports previous predictions [*Schultz*, 1992; *Barnouin-Jha and Schultz*, 1996] that a vortex ring generated during cratering on Mars could entrain considerable amounts of material. Although our laboratory experiments are conducted in a water tank, the three modes are plotted for a realistic range of wind (air) velocity (from a few to ~100 m/s) and of particle diameters (from a few 100 μm to ~10 mm) because dynamical similarity holds for the particle threshold problem. We should point out that although we match two dimensionless numbers based on particle scale (Re_p and θ_p) when we compare the laboratory to Mars, the Reynolds number based

Table 2. Parameters of the Present Martian Condition for Figure 3b[a]

Description of Parameters	Symbol	Value
Gravity acceleration, m/s²	g	3.711
Wind velocity, m/s	U	$1 \sim 100$
Martian Atmosphere (CO_2 Gas) at 215 K and 560 Pa		
Density, kg/m³	ρ_{flow}	1.4×10^{-2}
Kinematic viscosity, m²/s	ν	7.8×10^{-4}
Martian Atmosphere (CO_2 Gas) at 190 K and 140 Pa		
Density, kg/m³	ρ_{flow}	3.9×10^{-3}
Kinematic viscosity, m²/s	ν	2.4×10^{-3}
Martian Atmosphere (CO_2 Gas) at 230 K and 900 Pa		
Density, kg/m³	ρ_{flow}	2.1×10^{-2}
Kinematic viscosity, m²/s	ν	5.6×10^{-4}
Martian Surface Particles		
Density, kg/m³	$\rho_{particle}$	2.5×10^3
Diameter	d	$10 \ \mu m \sim 10 \ cm$

[a]We select the condition of 215 K/560 Pa as the general condition of Martian present surface. The condition of 190 K/140 Pa indicates the condition of 15 km high [*Carr*, 1996; *Zurek*, 1992] at which the ejecta of 30 km crater in diameter (maximum of DLE craters [*Barlow and Perez*, 2003]) can reach. We also draw the line of the condition of 230 K/900 Pa, the maximum value in Viking observation [*Zurek*, 1992], to indicate pressure dependence.

ejecta [e.g., *Schultz*, 1992] and/or a mixture of subsurface volatiles as liquid or vapor. The denser flow would have larger θ_p, so that, for example, a smaller U could transport particles of a given diameter. Higher atmospheric temperatures (lower density) due to early time heating of the atmosphere by the impact could counteract these higher densities, although strong return winds and any impact obliquity may minimize this heating [*Barnouin-Jha and Schultz*, 1996].

[18] In order to constrain the ancient Martian environment from our regime diagram (Figure 3b), we must know at least one of three unknown parameters: the density ρ_{flow}, the velocity of radial flow U, and the particle diameter d. Although it is hard to obtain ρ_{flow} and U from the existing observations, it may be possible to determine the particle size d. For instance, the range of particle diameter on the Martian surface could be estimated by analyzing thermal inertia from the images of Thermal Emission Imaging System (THEMIS). Future dedicated missions to Martian ejecta by a rover, or even a sample of ejecta returned by astronauts may further help in this.

References

Bagnold, R. A. (1941), *The Physics of Blown Sand and Desert Dunes*, 275 pp., Methuen, New York.

Barlow, N. G., and C. B. Perez (2003), Martian impact crater ejecta morphologies as indicators of the distribution of subsurface volatiles, *J. Geophys. Res.*, *108*(E8), 5085, doi:10.1029/2002JE002036.

Barlow, N. G., J. M. Boyce, F. M. Costard, R. A. Craddock, J. B. Garvin, S. E. H. Sakimoto, R. O. Kuzmin, D. J. Roddy, and L. A. Soderblom (2000), Standardizing the nomenclature of Martian impact crater ejecta morphologies, *J. Geophys. Res.*, *105*(E11), 26,733–26,738.

Barnouin-Jha, O. S., and P. H. Schultz (1996), Ejecta entrainment by impact-generated ring vortices: Theory and experiments, *J. Geophys. Res.*, *101*(E9), 21,099–21,115.

Barnouin-Jha, O. S., and P. H. Schultz (1998), Lobateness of impact ejecta deposits from atmospheric interactions, *J. Geophys. Res.*, *103*(E11), 25,739–25,756.

Barnouin-Jha, O. S., S. Baloga, and L. Glaze (2005), Comparing landslides to fluidized crater ejecta on Mars, *J. Geophys. Res.*, *110*, E04010, doi:10.1029/2003JE002214.

Boyce, J. M., and P. J. Mouginis-Mark (2006), Martian craters viewed by the Thermal Emission Imaging System instrument: Double-layered ejecta craters, *J. Geophys. Res.*, *111*, E10005, doi:10.1029/2005JE002638.

Carr, M. H. (1996), *Water on Mars*, 229 pp., Oxford Univ. Press, New York.

Carr, M. H., L. S. Crumpler, J. A. Cutts, R. Greeley, J. E. Guest, and H. Masursky (1977), Martian impact craters and emplacement of ejecta by surface flow, *J. Geophys. Res.*, *82*(28), 4055–4065.

Eames, I., and S. B. Dalziel (2000), Dust resuspension by the flow around an impacting sphere, *J. Fluid Mech.*, *403*, 305–328.

Greeley, R. (2002), Saltation impact as a means for raising dust on Mars, *Planet. Space Sci.*, *50*, 151–155.

Greeley, R., R. Leach, B. White, J. Iversen, and J. Pollack (1980), Threshold windspeeds for sand on Mars: Wind tunnel simulations, *Geophys. Res. Lett.*, *7*(2), 121–124.

Mouginis-Mark, P. (1981), Ejecta emplacement and modes of formation of Martian fluidized ejecta craters, *Icarus*, *45*, 60–76.

Sagan, C. (1975), Windblown dust on Venus, *J. Atmos. Sci.*, *32*, 1079–1083.

Sagan, C., and R. A. Bagnold (1975), Fluid transport on Earth and Aeolian transport on Mars, *Icarus*, 209–218.

Schultz, P. H. (1992), Atmospheric effects On ejecta emplacement, *J. Geophys. Res.*, *97*(E7), 11,623–11,662.

Wada, K., and O. S. Barnouin-Jha (2006), The formation of fluidized ejecta on Mars by granular flows, *Meteorol. Planet. Sci.*, *41*(10), 1551–1569.

Widnall, S. E., D. B. Blisse, and C. Y. Tsai (1974), The instability of short waves on a vortex ring, *J. Fluid Mech.*, *66*, 35–47.

Zurek, R. W. (1992), Comparative aspects of the climate of Mars: An introduction to the current atmosphere, in *Mars*, edited by H. H. Kieffer et al., pp. 799–817, Univ. of Ariz. Press, Tucson.

O. S. Barnouin-Jha, Johns Hopkins University Applied Physics Laboratory, 11100 Johns Hopkins Road, Laurel, MD 20723-6099, USA. (olivier.barnouin-jha@jhuapl.edu)

I. Kumagai, Institut de Physique du Globe de Paris, 4, place Jussieu, F-75252 Paris Cedex 05, France. (kumagai@ipgp.jussieu.fr)

K. Kurita and A. Suzuki, Earthquake Research Institute, University of Tokyo, 1-1-1, Yayoi, Bunkyo-ku, Tokyo, 113-0032, Japan. (kurikuri@eri. u-tokyo.ac.jp; ayako@eri.u-tokyo.ac.jp)

Y. Nagata, Department of Applied Physics, Tokyo University of Agriculture and Technology, 2-24-16, Nakamachi, Koganei, Tokyo, 184-8588, Japan. (nagata@cc.tuat.ac.jp)